CONFERENCE PRE-PRINT

THERMAL QUENCH DYNAMICS AND HEAT FLUX DISTRIBUTION DURING MASSIVE-IMPURITY-INJECTION TRIGGERED DISRUPTION IN EAST

L. ZENG

Department of Engineering Physics, Tsinghua University

Beijing, China

Email: zenglong@tsinghua.edu.cn

W. XIA, Y.SUN, T. TANG, S. ZHAO, T. SHI, D. CHEN, Y. DUAN, L. XU, G. LI, G. ZUO, J. HU, X. GAO Institute of Plasma Physics, Chinese Academy of Sciences

Hefei, China

D. HU

School of Physics, Beihang University Beijing, China

X. ZHU

Advanced Energy Research Center, Shenzhen University Shenzhen, China

Z. GAO

Department of Engineering Physics, Tsinghua University Beijing, China

the JOREK Team*

*See Hoelzl et al 2024 (https://doi.org/10.1088/1741-4326/ad5a21) for the JOREK Team

Abstract

Thermal quench (TQ) dynamics in massive-gas-injection (MGI) triggered EAST disruptions, including reversion of magnetic-island's rotation direction in the pre-TQ phase, staged cooling and 3D splitting of heat flux during the TQ phase, have been experimentally demonstrated. Neoclassical theory shows the radial electric field induced by the parallel viscosity transition after impurity injection could cause the mode rotation transition, and 3D non-linear JOREK simulations present heat stripes are attributed to mode-induced additional magnetic connections to the divertor. These findings can enhance the understanding of the impurity influx and the heat flux deposition during mitigated disruptions.

1. INTRODUCTION

Major disruptions pose serious challenges to the safe operation of tokamaks. One such challenge is the thermal quench (TQ) process, which can generate significant thermal load on the plasma-facing components (PFCs). During TQ, the deposited heat loading on the divertor targets is proportional to the stored thermal energy, inversely proportional to the duration of TQ (~ 1 ms in ITER) and effective divertor target area. TQ durations can vary significantly due to multiple disruptions, but the initial first stage time (τ_{1-2}) and the final second stage time (τ_2) still roughly follows that $\tau_{1-2} \sim a^{1.5}$ and $\tau_2 \sim a^1$, in which a is the plasma minor radius [1]. Note that not all TQs exhibit clear two stages, and a single step is explained as the overlap of two stages presumably or the lack of a sufficiently large second stage. The rapid loss of total thermal energy over a very short timescale is caused by the global stochastic field generated by the overlapping of magnetic islands with different helicities. However, the formation of a stochastic field is not instantaneous, and complex magnetohydrodynamic (MHD) phenomena often accompany the TQ process.

To avoid the disruption-induced damage, various disruption mitigation techniques such as massive gas injection (MGI) and shattered pellet injection (SPI) have been implemented in many devices. The operating principles of both the MGI and SPI techniques involve injecting numerous impurity atoms to radiate stored plasma energy, thus preventing this energy from directly impacting the PFCs and, hence, protecting them. Despite their shared working principles, SPI is superior to MGI and is hence emerging as a promising replacement for MGI in the disruption mitigation systems (DMSs), due to deeper penetration into the plasma and more symmetric radiation power.

2. DISRUPTION MITIGATION AND TYPICAL TQ PROCESS ON EAST

Both MGI and SPI technologies have been developed for disruption mitigation on EAST. The MGI system relies on a fast valve and the response time of the valve is as short as 0.15 ms. The noble gas, including helium, neon and argon, can be used via the MGI system and the maximum amount of the gas is ~ 20 kPa L [2]. In the SPI system, pure neon cylindrical pellets and mixed neon-hydrogen pellet can be used with an injection speed < 400 m s⁻¹ [3].

Intended disruption triggered by SPI and MGI have been done on EAST and the comparative results are shown in figure 1. While MGI tends to deposit more impurities at the edge, SPI penetrates deeper into the plasma and results in a shorter overall disruption duration. The trajectory of impurities exhibits strong asymmetry in both toroidal and poloidal direction. Interestingly, no clear difference in TQ process has been found in two types of disruptions [4].

Timescale of TQ during disruptions on EAST tokamak has been examined by ECE and SXR diagnostic systems [5]. The TQ duration of major disruptions (MDs) is within 56-788 µs. The lower bound of TQ duration, indicating the minimum durations at different current plateaus, decreases as plasma current increases. This decrease is due to the connection length shortening and the plasma temperature increasing. For MDs, two typical TQ processes, single-

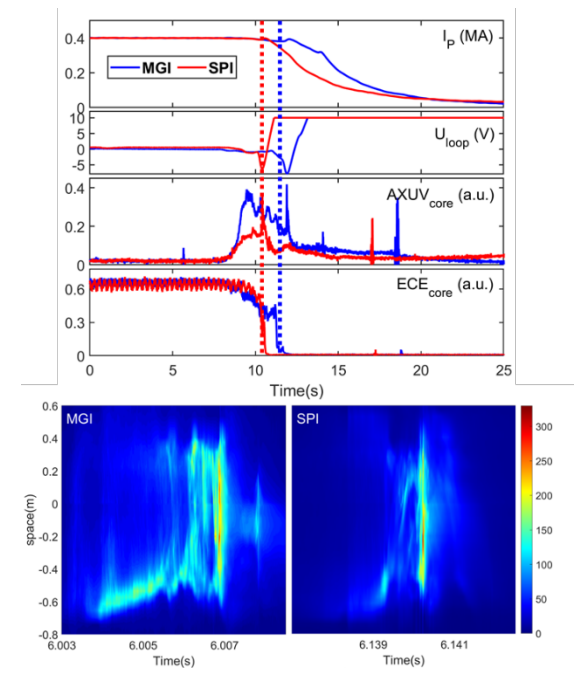


Fig. 1. From top to bottom: evolution of the plasma current, loop voltage, edge AXUV signal, core ECE signal and AXUV contour maps by MGI (left) and SPI (right), obtained from AXUV measurements.

stage TQ and double-stage TQ, are characterized by different magnetic perturbations. In the case of single-stage TQ, fast loss stage is triggered by magnetic perturbation exceeding 4.3×10^{-3} T with a fast growth rate 1.5×10^{-2} µs⁻¹. In contrast, fast quench is triggered by a slightly smaller magnetic perturbation 3.6×10^{-3} T in double-stage TQ, and the growth rate 5.3×10^{-3} µs⁻¹ is an order of magnitude smaller than single-stage TQ. Since the whole process of TQ energy release can be divided into the transport in a stochastic field within separatrix and in scrape-off layer, and according to the typical parameters of EAST, TQ duration in MDs is roughly estimated to be 245 µs by approximate formula, which is consistent with the experimental results.

3. IMPURITY TRANSPORT DURING MASSIVE-IMPURITY INJECTION TRIGGERED DISRUPTIONS

When the MGI or SPI is triggered during the experiments, the impurity particles exhibit complex behaviour. According to simulations, initially, these particles move inward along the major radius due to their initial velocity. However, once the neutral particles are ionized and constrained by the local field, the impurities are deposited at $\Psi_N \sim 0.7$ on EAST and cannot directly penetrate into the core plasma. Subsequently, the impurity particles, following magnetic field lines, extend along the field, creating new deposition spots at different poloidal positions on the same magnetic surface [6]. On EAST experiments, a new phenomenon following impurity injection, rotation direction reversion of magnetic island, has been observed [4]. This reversal appears to be tightly linked to changes in plasma rotation and likely couples to impurity transport.

3.1. Enhanced inward transport of impurities

3.1.1. Experimental observation

Rotation direction of magnetic island is observed to reverse in the pre-TQ phase when large amounts of neon are injected into co-current NBI-heating plasmas, as shown in Fig. 2(a). After impurity injection at 6 s, the 2/1 mode's rotation slows down and then reverses from the ion diamagnetic to the electron diamagnetic direction. The mode frequency changes from 2 kHz to -2 kHz in <0.5 ms. Furthermore, more impurity injection can enhance the reversal process. Meanwhile, similar geometrical structure of impurity radiation has been observed in bolometer measurement, shown in Fig. 2(b). The radiation is initially localized near the plasma boundary after impurity injection. However, the radiation in the core region significantly increases following the rotation direction of the

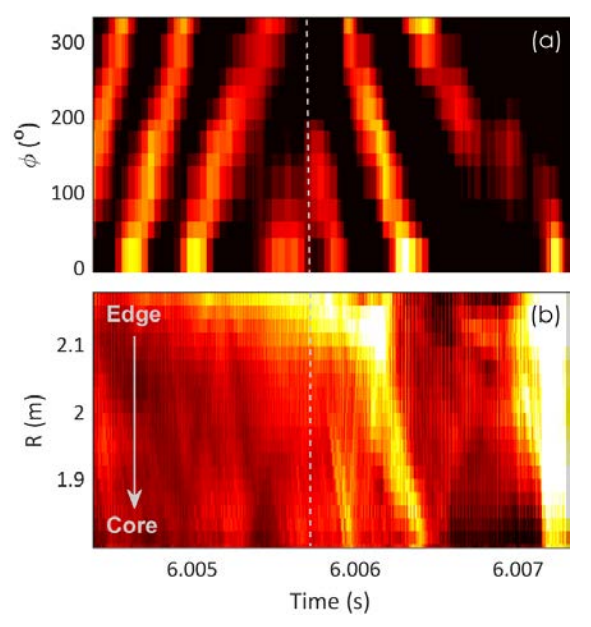


FIG. 2. (a) Time evolution of n=1 MHD modes, and (b) contour plot of bolometry measurements. The dashed line indicates time for rotation reversion.

mode reversed. These results suggests that the impurity penetration accompanied by mode rotation could lead to inward plasma cooling.

To estimate impurity trajectory more clearly, the 2D SXR arrays and AXUV arrays are employed and the impurity influx can be divided into two stages. As shown in figure 2(b), the vertical AXUV chords indicate a burst of impurity penetration concurrent with the reversal. Prior to the reversal, impurities hardly reach the core and predominantly accumulate near the edge, outside of q=2 surface. Impurities are observed to drift along ion diamagnetic direction, which is dependent on position of injection. Inward pinch speed is estimated as ~60 m/s. Immediately after reversal, a mechanism develops that rapidly drives impurities inward into the core plasma. Drift direction of impurities changes to electron diamagnetic direction and the inward pinch speed is up to 300 m/s.

Figure 3 compares the n=1 island rotation for different injected gas amounts. The frequency transitions from the ion-diamagnetic sign ($\sim+3$ kHz) to the electron-diamagnetic sign (~-3 kHz) within hundreds of

microseconds. With increasing injection, the transition occurs earlier and more abruptly. The initial ion-diamagnetic frequency is driven by co-NBI heating. Similar trends are also found in RF-heating discharges, where the n=1 frequency shifts from ~ -5 kHz to ~ -9 kHz after argon injection. In Fig. 3(b), the poloidal mode number remains primarily m=2 throughout the transition, which rules out changes in island mode structure as the cause. Frequencies from direct peak counting agree with toroidal array inferences, validating the analysis. Overall, the increase in magnitude toward the electron-diamagnetic direction is robust and insensitive to the injected species, heating methods, or toroidal field direction.

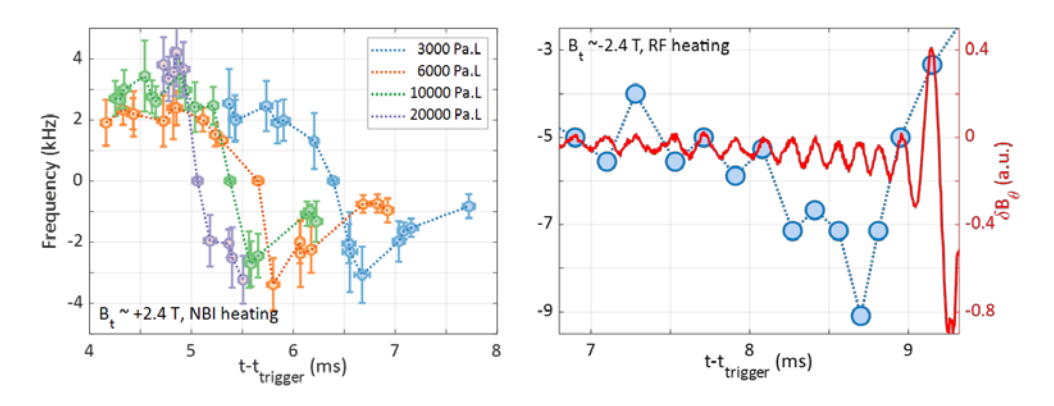


FIG. 3. Dependence of frequency change of tearing mode on the gas species and numbers of impurities (left), and heating methods (right).

3.1.2. Data analysis and modelling

Tearing mode is mainly determined by electron dynamics. In the flux-surface coordinate, the n=1 mode frequency can be written as [7]

$$2\pi \cdot f_{\text{MHD}} = \Omega_{E \times B} + \Omega_{*e} + 0.71\Omega_{*Te}$$

where $\Omega_{E \times B}$ is $E \times B$ frequency, Ω_{*e} is electron diamagnetic frequency and Ω_{*Te} comes from heat friction force. Here $\Omega_{E \times B}$ can be determined by ion radial force balance equation

$$\Omega_{E\times B} = \boldsymbol{U}\cdot\nabla\zeta - q\boldsymbol{U}\cdot\nabla\theta - \Omega_{*i}$$

where $\mathbf{U}\cdot\nabla\zeta$ is the toroidal angular frequency, $\mathbf{U}\cdot\nabla\theta$ is the poloidal angular frequency and $\Omega_{^{\circ}i}$ is ion diamagnetic frequency. Note that time scale of frequency change (< 0.5 ms) is much less than τ_E (50-100 ms) on EAST, so the change of mode frequency is mainly caused by poloidal angular frequency. We therefore attribute the observed frequency change toward the electron-diamagnetic sign to the development of a negative radial electric field. For a 2/1 island on EAST, $E_r \sim -10$ kV/m, which in turn can drive impurity ions inward [8]. As for the plasma poloidal rotation, the neoclassical relaxation time in the collisional regime is $\tau_\theta \simeq q^2 R^2 \nu_i / \nu_{T_i}^2$. This expression gives $\tau_\theta \sim 0.1$ ms for our experimental parameters. Thus, the neoclassical theory can be applied to explain poloidal rotation in the EAST tokamak.

To determine U_{θ} , we solve the poloidal moment equation. In standard neoclassical theory, the poloidal momentum is damped by the poloidal (parallel) viscosity. However, the poloidal rotation can be driven by the parallel viscosity associated with the collisionality and impurity. The poloidal momentum balance includes pressure, viscosity, friction, and damping terms. During the transition, the central temperature is roughly constant and the timescale is extremely short, indicating that pressure-gradient drive term is not dominant. The key parameter is the parallel viscosity (governing poloidal flow). In the classical KDG model considering the balance between parallel viscosity and friction, the steady poloidal flow is derived assuming fully developed neoclassical flow [9]. However, this assumption is not valid here because the toroidal rotation cannot relax on sub-millisecond timescales. We therefore adopt a time-scale separation: the poloidal flow rapidly equilibrates while the toroidal rotation is effectively frozen (as in L–H transition analyses [10]). In this picture, the system transiently adjusts radial electric field to balance parallel viscosity against friction, yielding a transient intermediate neoclassical state.

With fixed toroidal rotation assumption, the main ion poloidal velocity is:

$$u_{0\theta}^{i} = \frac{U_{0\parallel}^{i}}{B} + \frac{B_{T}T_{i}}{e_{i}B^{2}} \left(\frac{L_{pi}^{-1}}{B_{p}} - \frac{e_{i}}{T_{i}}\frac{E_{r}}{B_{p}}\right)$$

And the equation set are shown as the below:

$$\begin{bmatrix} \frac{n_{l}m_{l}\tau_{ii}}{n_{l}m_{l}\tau_{ii}}\mu_{00}^{l} + \alpha & \frac{n_{l}m_{l}\tau_{ii}}{n_{l}m_{l}\tau_{ii}}\mu_{01}^{l} & \alpha\frac{B_{T}}{B_{p}} & -1.5\alpha \\ \frac{n_{l}m_{l}\tau_{ii}}{n_{l}m_{l}\tau_{II}}\mu_{10}^{l} & \frac{n_{l}m_{l}\tau_{ii}}{n_{l}m_{l}\tau_{II}}\mu_{11}^{l} + \alpha\frac{T_{i}}{T_{l}}(7.5 + \sqrt{2}\alpha x^{-1}) & 0 & -6.75\alpha x^{2} \\ -\alpha & 0 & -\mu_{00}^{i}\frac{B_{T}}{B_{p}} - \alpha\frac{B_{T}}{B_{p}} & \mu_{01}^{i} + 1.5\alpha \\ -1.5\alpha & -6.75\frac{T_{i}}{T_{l}}\alpha x^{2} & -\mu_{10}^{i}\frac{B_{T}}{B_{p}} - 1.5\alpha\frac{B_{T}}{B_{p}} & \mu_{11}^{i} + (\sqrt{2} + 3.25\alpha) \end{bmatrix} \begin{bmatrix} u_{10}^{l}B^{2} \\ u_{10}^{i}B^{2} \\ E_{r} \\ u_{10}^{i}B^{2} \end{bmatrix}$$

$$= \begin{bmatrix} \alpha\frac{B_{T}T_{l}}{e_{l}B_{p}L_{pl}} + \alpha U_{01}^{i}B + 1.5\alpha\frac{B_{T}T_{i}}{B_{p}e_{l}L_{Ti}} \\ \alpha\frac{T_{i}}{T_{l}}(7.5 + \sqrt{2}\alpha x^{-1})\frac{B_{T}T_{l}}{B_{p}e_{l}L_{Tl}} + 6.75\alpha x^{2}\frac{B_{T}T_{i}}{B_{p}e_{i}L_{Ti}} \\ -\mu_{00}^{i}U_{01}^{i}B - \mu_{10}^{i}\frac{B_{T}T_{i}}{e_{l}B_{p}L_{pi}} - \alpha U_{01}^{i}B - 1.5\alpha\frac{B_{T}T_{i}}{B_{p}e_{l}L_{Ti}} - \alpha\frac{B_{T}T_{l}}{B_{p}e_{l}L_{Tl}} \\ -\mu_{10}^{i}U_{01}^{i}B - \mu_{10}^{i}\frac{B_{T}T_{i}}{B_{p}e_{l}L_{pi}} - 1.5\alpha U_{01}^{i}B - (\sqrt{2} + 3.25\alpha)\frac{B_{T}T_{i}}{B_{p}e_{i}L_{Ti}} - 1.5\alpha\frac{B_{T}T_{l}}{e_{l}B_{p}L_{pl}} + 6.75\frac{T_{i}}{T_{l}}\alpha x^{2}\frac{B_{T}T_{l}}{B_{p}e_{l}L_{Tl}} \end{bmatrix}$$

where the impurity strength parameter $\alpha = n_i Z_i^2/n_i Z_i^2$, and $x = V_{th,I}/V_{th,i} << 1$. Previous JOREK simulations show that after impurity injection the local impurity density and collisionality near q = 3 rise rapidly, which strongly affects viscosity. We therefore can estimate nonlinear change of the radial electric field by scanning collisionality and impurity strength.

Collisionality controls parallel viscosity via its effect on the particle orbit regime. In Fig. 4, as the ion collisionality increases, the radial electric field grows in the negative direction and reaches approximately 25 kV m⁻¹. The dark solid curve denotes an asymptotic composite expression that connects the Hirshman–Sigmar viscosity across banana, plateau, and Pfirsch–Schlüter (P–S) regimes. Because this composite is less accurate in the plateau regime, we also present results using the banana-regime and P–S-regime formulas separately. The calculations show that, if the main ions remain in the banana regime, the electric field exhibits no significant growth. The transition from

banana to P–S is what drives the change in electric field. The discrepancy between the composite and the single-regime curves further indicates that the regime transition can be sharper than suggested by the asymptotic formular. Physically, as collisionality increases, the viscous coefficient decreases; to maintain the viscosity–friction balance, the required $\mathbf{E} \times \mathbf{B}$ response strengthens, producing a more negative electric field. We further evaluate radial electric field versus impurity collisionality at fixed ion collisionality. The response is weaker than in the ion-collisionality scan, which is plausibly attributable to the dependence of the thermal-friction contribution on the ratio $V_{\text{th,I}}/V_{\text{th,i}}$.

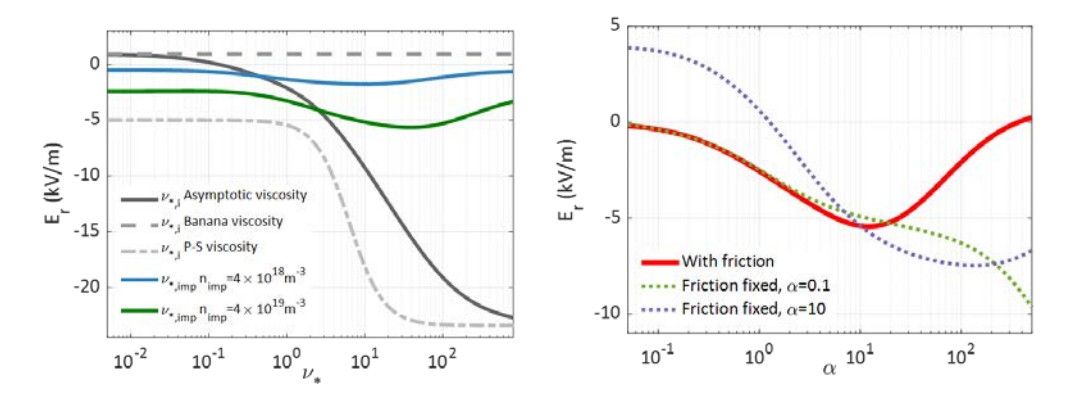


FIG. 4. Dependence of radial electric field on collisionality (left) and impurity strength (right)

Impurity strength modifies both the banana and P–S viscosities even at fixed collisionality, and it also changes the friction. We therefore isolate the effect of impurity strength while holding the collisional frequency constant. As shown in Fig. 4, the viscosity remains sensitive to impurity strength: impurity orbits perturb ion orbits and thereby alter the effective viscosity. Friction limits the growth of the negative electric field. The turning point of electric field set by the relative magnitude of viscosity versus friction under these conditions. After impurity injection, the impurity density can rise rapidly, which motivates a dedicated impurity-density scan. The radial electric field grows quickly at low impurity strength. Comparing the red curves in Fig. 4(right), the early increase is primarily due to impurity-induced changes in the ion viscosity through orbit disturbing, whereas the later growth is driven by the collisionality parameter that further modifies viscosity. Note that the actual growth should be sharper than depicted. The asymptotic composite tends to smooth intrinsically abrupt regime transitions, as discussed above. Cases with higher impurity temperature display a faster dependence on impurity strength. Cases with higher impurity charge produce a larger electric filed amplitude, although the variation with strength becomes more gradual.

Global effects with massive impurity injection show that the main-ion poloidal velocity is directed toward the ion-diamagnetic side, whereas the impurity poloidal velocity is directed toward the electron-diamagnetic side, consistent with the result reported by Kim [9,11]. Variations in the main-ion poloidal flow are governed by the $\mathbf{E} \times \mathbf{B}$ drift. For impurities, both the parallel flow and the $\mathbf{E} \times \mathbf{B}$ velocity make comparable contributions. In addition, the magnitude of the radial electric field increases as the ion-temperature gradient steepens.

In summary, the increase of radial electric field toward the negative direction is predominantly caused by ion-impurity collisions that disturb main-ion orbits and reduce the main-ion parallel viscosity. To re-establish the balance between viscosity and friction, the plasma strengthens the $\mathbf{E} \times \mathbf{B}$ response, yielding a more negative E_r . For typical parameters we obtain $E_r \sim 8$ kV/m, close to the experimental estimate of about -10kV/m. The actual variation is likely stronger than that predicted by the asymptotic composite, which intrinsically smooths regime transitions. In addition, neither the temperature nor the effective charge remains strictly constant during injection, increasing the collision frequency. Together, these effects naturally produce a sharp transition in the calculations, comparable to that observed experimentally.

3.2. Asymmetrical expansion of neon impurities in toroidal direction

JOREK is a 3D nonlinear extended MHD code widely used to study large-scale plasma instabilities in realistic divertor tokamaks [12]. In our JOREK simulations, we employed a single-fluid reduced MHD model with a non-equilibrium impurity treatment. The JOREK simulation commences with the reconstruction of the initial equilibrium, employing the Grad-Shafranov equation. The electron temperature, electron density, and EFIT output file, comprising magnetic surface data, are then introduced as inputs into JOREK.

In the initial equilibrium $q_{min} > 1.5$, consistent with experimental observations. This setup provides insights into TQ process in the absence of q = 1 surface in EAST. Following the initialization, the plasma evolves for approximately~584 μ s to establish scrape off layer (SOL) flow. In our simulations, the neon particle flux is set to $6 \times 10^{22} \, \mathrm{s}^{-1}$, which is represented by a simple Gaussian source term at the midplane over a duration of 5 ms, and is modelled by approximately by 2×10^7 super-particles in most cases. Specially, the Gaussian source has 5 cm

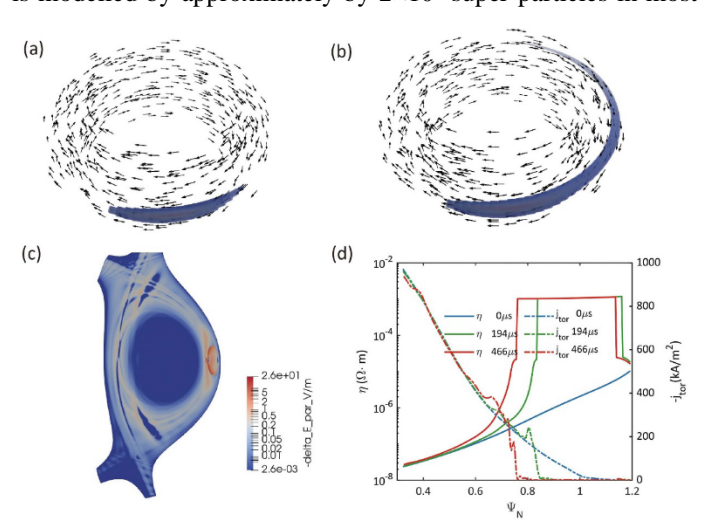


FIG. 5. (a) and (b) show the 3D distribution of neon impurities in case 1 at 194 μ s and 466 μ s, respectively, with black arrows indicating magnetic vectors. (c) In the cross-section of $\phi = 0^{\circ}$, the variation in the parallel electric field is illustrated, defined as $-\delta E_{||} = E_{||}(t=0 \ \mu s) - E_{||}(t=466 \ \mu s)$. Only regions where $-\delta E_{||} > 0$ are colored due to the use of logarithmic coordinates. (d) Resistivity and toroidal current density profiles at various times along $\psi_N = 0.3-1.2$ with Z = 0.1 m.

poloidal expansion and are located at a toroidal angle of $\phi=0$ without any toroidal expansion. These particles are injected perpendicular to the magnetic surface at a speed of 2000 m s⁻¹.

During the JOREK simulation, we found that the toroidal expansion of neon impurities is not symmetric. The impurity particles drift opposite to the magnetic field vectors near the plasma edge, which is driven by a parallel electric field E_{\parallel} of approximately 30 V/m. Prior to injection, the maximum E_{\parallel} is roughly 0.1 V/m. The change of E_{\parallel} is shown in fig. 5, where it increases primarily at the plasma edge, particularly in the impurity deposition region. A similar parallel electric field behavior was also observed in NSTX non-equilibrium radiation simulations using the M3D-C1 code [13]. The parallel electric field is expressed as $E_{\parallel} = \eta(T_e, Z_{eff}) \cdot j_{tor}$. Massive neon gas injection rapidly cools the local plasma, lowering the temperature to the minimum cut-off value, resulting in a saturation resistivity plateau. Notably, a small amount of plasma current remains at the resistivity plateau, indicating that the current relaxation time is longer than

the resistivity increase time. The rapid rise in resistivity may be attributed to the non-equilibrium radiation treatment, which better captures the initial cooling phase, while coronal equilibrium radiation treatment tends to underestimate this process [14].

4. INTERPRETIVE JOREK SIMULATION OF THERMAL QUENCH

Staged cooling in the TQ phase, mainly including the single-stage TQ and double-stage TQ, has been identified in EAST disruptions [5]. A single-stage TQ is characterized by a faster growth rate $(1.5 \times 10^{-2} \ \mu s^{-1})$ of MHD activities compared to a double-stage TQ $(5.3 \times 10^{-2} \ \mu s^{-1})$. In a double-stage TQ, the thermal energy loss time becomes shorter with increased impurity, leading to the merging of the 1-2 delay stage and the fast quench stage into a single-stage TQ. JOREK simulation has reproduced both the double-stage and single-stage TQ process by varying impurity particle fluxes.

In the typical simulation case, a double-stage-like TQ process is reproduced in the electron temperature evolution. The first core temperature collapse begins at approximately 850 μ s, followed by the onset of the fast quench at around 1400 μ s. The edge temperature collapses first, followed by the growth of magnetic islands, which leads to core thermal energy loss and the formation of a temperature plateau. Additionally, the core energy loss, indicating an outward heat flux, results in temperature peaks in the outer regions. Similar temperature peaks have also been observed in experiments. These two temperature collapses are triggered by MHD activities. During the initial nonlinear phase at $t_1 = 850~\mu$ s, high-n harmonics first grow and interact, competing with one another. Among them, the n=1 harmonic reaches its peak amplitude $\sim 1 \times 10^{-4}$ ahead of the others. The m/n=3/1, 4/1, 5/1 modes in plasma edge grow to a comparable amplitude and primarily contribute to the edge stochasticity. Besides, the growth of the 2/1 island weakens core confinement during the first collapse phase. Subsequently, the 5/2 mode emerges, driven by the nonlinear coupling between the 2/1 and 3/1 modes. However, these nonlinear interactions only lead to the formation of a stochastic sandwich layer, resulting in a little core energy loss. During the fast quench phase, the further growth of the 2/1 magnetic island couples with the 3/1 mode, while higher harmonics, such as 6/3, also contribute to the global stochasticity. Note that the excitation of higher harmonics results from the mismatch between the impurity deposition location and the magnetic island O-point, particularly when there

is a poloidal shift of the plasma. In the experiment, higher harmonics are expected to be more prevalent, as the gas valve position remains fixed, whereas the plasma undergoes an initial poloidal rotation.

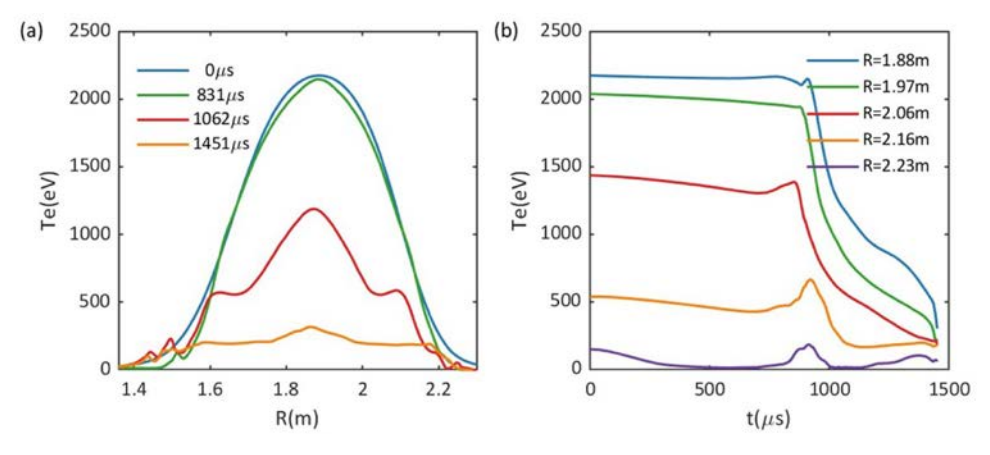


FIG. 6. (a) Electron temperature profile along a line with $Z=0.1\,$ m at different times. (b) Electron temperature evolution at different radial positions in the simulation case.

Comparing the MHD modes observed in simulations with the experimental modes measured by Mirnov coils is valuable. The n=1 mode in the toroidal signals grows significantly before the TQ, which aligns with the simulation results. Additionally, the toroidal oscillation period increases rapidly, indicating a gradual locking of modes by the fixed gas source. In terms of the energy spectrum, cases with a greater quantity of injected gas particles exhibit a more rapid growth rate of the n=1 mode, which has been verified in the experiment.

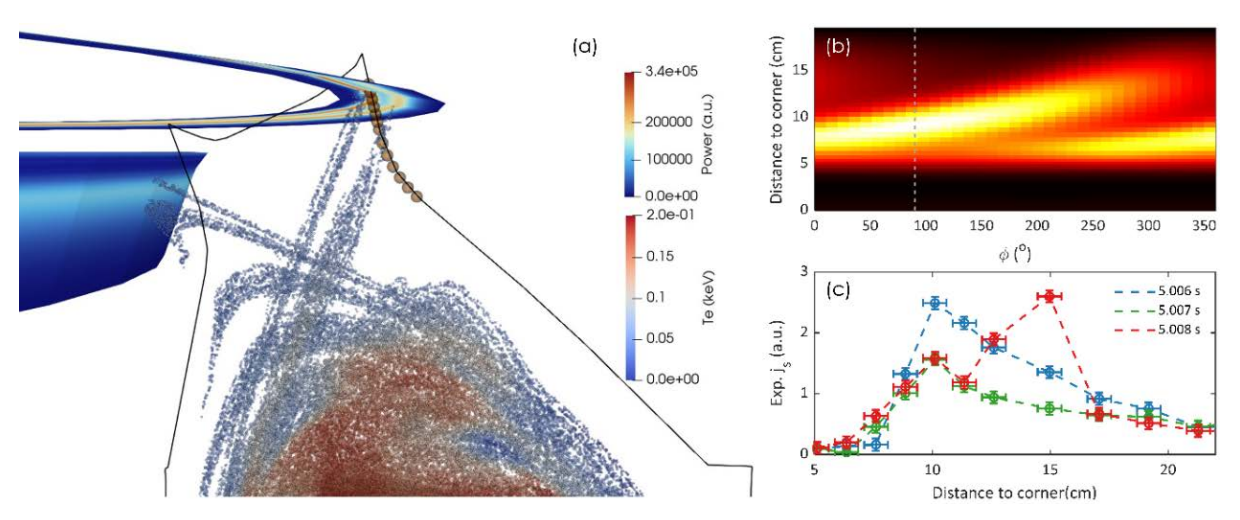


FIG. 7. (a) Poincaré plot of the magnetic topology and the resulted strike point splitting on the divertor; (b) 3D parallel convective particle flux orthogonal to the upper-outer target. The dashed line indicates the toroidal position measured in the experiment; (c) saturated ion flux obtained by the array of Langmuir probes on the upper-out divertor.

Strike point splitting on the divertor during the TQ has been detected by the array of Langmuir probes, shown in Fig. 7(c). After impurity injection, the saturated ion flux (j_s) at 5.007 s is initially measured to decrease, which may be attributed to a reduction in parallel fluid velocity caused by the injected cold gas. Then, a clear splitting of strike point has been found during the TQ (5.008 s), and j_s on the second strike-point is even larger than the original strike point. This observation could be understood by 3D effects of MHD activities during the TQ. The JOREK simulation presents that MHD modes change magnetic topology and result in strike point splitting near the upper X-point, shown in Fig. 7(a). The bifurcation occurrence of strike point strongly relates to the mode amplitude. The unstable manifolds form two large lobes near the upper-outer divertor, which intersect the divertor target and split the strike point into double stripes. Fig. 7(b) demonstrates that the simulated parallel convective particle flux at the upper-outer target, combined with the strike-point splitting, exhibits an n = 1 structure. The simulation results for the upper-outer target consists well with experimental observations, showing the impact of double lobes on local particle transport. This result provides an explanation for the broadening of energy deposition width during the TQ in ASDEX Upgrade and JET [15,16].

5. CONCLUSION

Thermal quench (TQ) dynamics in massive-gas-injection (MGI) triggered EAST disruptions have been experimentally demonstrated in experiments and simulations. (1) Quick change in mode frequency: Quick change in mode frequency is explained by the collisionality transition from banana regime to P–S regime, caused by massive impurity injection. The radiation in the core region significantly increases following the change. (2) staged cooling: The 3/1 mode couples with the 4/1 and 5/1 modes, contributing to edge stochasticity. The nonlinear interaction between the 3/1 and 2/1 modes primarily leads to global stochastic. (3) 3D splitting of heat flux: The parallel convective particle flux at the upper-outer target, combined with the strike-point splitting, exhibits an n=1 structure.

ACKNOWLEDGEMENTS

This work was supported by the National Key R&D Program of China under Contract (No. 2024YFE03010000), the Strategic Priority Research Program of Chinese Academy of Sciences (No. XDB0790203), and National Natural Science Foundation of China (Nos. 12475225 and 12405269). The work was carried out at National Supercomputer Center in Tianjin, and the calculations were performed on Tianhe new generation supercomputer. We thank the staff members at EAST in Hefei (https://cstr.cn/31130.02.EAST), for providing technical support and assistance in data collection and analysis.

REFERENCES

- [1] ITER Physics Expert Group on Disruptions, Plasma Control, and MHD and ITER Physics Basis Editors, Chapter 3: MHD stability, operational limits and disruptions, Nucl. Fusion **39** (1999) 2251–2389.
- [2] Zhuang, H., Zhang, X., Fast valve based on double-layer eddy-current repulsion for disruption mitigation in Experimental Advanced Superconducting Tokamak, Rev. Sci. Instrum. **86** (2015) 053502
- [3] Yuan J., Zuo G., Zhao S., Design of a shattered pellet injector and preliminary bench tests of Ne pellet formation for EAST disruption mitigation, Fusion Eng. Des. **191** (2023) 113567.
- [4] Zhao, S., Yuan, J., Zhuang, H., Characteristics of plasma disruption mitigation achieved by MGI and SPI on EAST, Nucl. Fusion **65** (2025) 016048.
- [5] Xia, W., Zeng, L., Tang, T., The timescale of thermal quench during disruptions in EAST, Plasma Phys. Control. Fusion **65** (2023) 085011.
- [6] Xia, W., Hu, D., Zeng, L., Interpretive JOREK simulation of thermal quench triggered by massive gas injection in EAST disruptions, Nucl. Fusion **65** (2025) 056028.
- [7] Sun Y., "Note on MHD mode frequency", private communication, 2025.
- [8] Stringer T.E., Neoclassical transport in the presence of fluctuations, Nucl. Fusion 32 (1992) 1421–1432.
- [9] Kim Y., Diamond P., Groebner R., Neoclassical poloidal and toroidal rotation in tokamaks, Phys. Fluids B: Plasma Phys. **3** (1991) 2050–2060.
- [10] Shaing K., Crume E., Bifurcation theory of poloidal rotation in tokamaks: A model for L–H transition, Phys. Rev. Lett. **63** (1989) 2369–2372.
- [11] Kim J., Burrell K., Gohil P., Rotation characteristics of main ions and impurity ions in H-mode tokamak plasma, Phys. Rev. Lett. **72** (1994) 2199–2202.
- [12] Hoelzl M., Huijsmans G., Pamela S., The JOREK non-linear extended MHD code and applications to large-scale instabilities and their control in magnetically confined fusion plasmas, Nucl. Fusion **61** (2021) 065001.
- [13] Ferraro N., Lyons B., Kim C., 3D two-temperature magnetohydrodynamic modeling of fast thermal quenches due to injected impurities in tokamaks, Nucl. Fusion **59** (2019) 016001.
- [14] Hu D., Huijsmans G., Nardon E., Collisional-radiative non-equilibrium impurity treatment for JOREK simulations, Plasma Phys. Control. Fusion **63** (2021) 125003.
- [15] Herrmann A., Eich T., Rohde V., ASDEX Upgrade Team, Power deposition outside the divertor in ASDEX Upgrade, Plasma Phys. Control. Fusion **46** (2004) 971–979.
- [16] Andrew P., Alonzo A., Arnoux G., First measurements of main chamber power load during JET disruptions, J. Nucl. Mater. **363–365** (2007) 1006–1010.